第 50 卷 第 14 期/2023 年 7 月/中国激光 研究论文

中国激光

基于双螺旋微纳光纤耦合器的光学游标传感特性研究

李玉洁，罗彬彬*，邹雪，石胜辉，范俊豪，吴德操，陈荟吉，杨翔文，古洪，赵明富**

重庆理工大学光纤传感与光电检测重庆市重点实验室，重庆 400054

摘要 针对双螺旋结构微纳光纤耦合器（DHMC），理论研究其游标效应的内在机理和光谱特性。实验制备直径为5~7 μm的DHMC，并研究其应变、温度以及折射率的传感特性，采用快速傅里叶变换（FFT）并利用带通滤波对特征干涉光谱数据进行提取，分别得到在x、y正交偏振态下的干涉光谱以及它们叠加形成的游标光谱。实验结果表明：制备的DHMC的结构参数及光谱特性与基于理论分析的预测基本吻合；DHMC的x、y偏振态干涉谱叠加形成的游标效应光谱与x、y正交偏振态下的干涉光谱相比较，对应变和温度传感呈现出减弱的光学游标效应，而对折射率传感则呈现出增强的光学游标效应。以上研究结论对DHMC的制备及其在折射率、温度及应变传感中的应用具有实际指导意义。

关键词 光纤光学；光纤传感器；双螺旋微纳光纤耦合器；折射率；温度；轴向应变

中图分类号 TN253 **文献标志码** A **DOI:** 10.3788/CJL221045

1 引 言

光纤传感器以其结构紧凑、灵敏度高、抗电磁干扰能力强等特点，在环境、工业、土木工程、生物医学、化工、航空航天等领域得到广泛应用[1-4]。微纳光纤具有微纳尺寸、极强倏逝场等优点，且易制备、易集成。各种微纳光纤干涉仪[5]、微纳光纤Bragg光栅[6]、微纳光纤耦合器（OMC）[7]、微纳光纤谐振器[8]等器件已被广泛研究，其中OMC是一种由两根单模光纤（SMF）熔融拉锥制成的微纳器件。2013年，Bo[9]提出了基于OMC的折射率传感器，在折射率（RI）为1.3340~1.3800的范围内平均RI灵敏度为2723 nm/RIU。2018年，Li等[10]研究了OMC在色散拐点附近的光谱特性和折射率敏感特性，表明OMC传感器直径为1.8 μm时，在RI为1.333附近时具有59624 nm/RIU的超高RI灵敏度，但由于传感器直径十分微小，增加了制作和操作的难度。

通过光学游标效应可直接放大光纤传感器的灵敏度，已有将该效应用于测量气体压力[11]、温度[12-13]、应变[14]、折射率[15-17]等的相关研究。但是这些光纤游标传感器是由两个级联或并联的光纤干涉仪组成，其中一个作为传感干涉仪，另一个作为参考干涉仪，由两个干涉仪的光谱叠加产生一个游标包络光谱，通过测量其中心波长漂移来检测外部参量。2018年，Li等[18]提出直径为3.2 μm的双螺旋微纳光纤耦合器（DHMC），获得35823.3 nm/RIU的RI灵敏度。由于DHMC本身具有类似游标的包络光谱，不需要再额外组合另一个参考干涉仪，因此与传统的光学游标效应传感器相比，其结构简单得多。2020年，Chen等[19]制作腰径为3.4 μm且具有游标效应的DHMC，在1.3333~1.3394的RI范围内最大灵敏度为27326.59 nm/RIU。这两个研究都从理论和实验上验证了DHMC的游标效应，分析了DHMC用于折射率传感增敏的原理，但是没有进一步分析DHMC所产生的游标包络受到的温度、应变等外部参量的影响。

本文将从理论和数值模拟两方面详细研究DHMC游标光谱的特性，并通过实验研究分析DHMC所产生的游标包络的折射率、温度及应变传感特性。为进一步得到DHMC在x和y两个正交偏振态下的灵敏度，应用数据处理的方法，先对干涉光谱进行快速傅里叶变换（FFT）找出最主要的两个频率分量，利用带通滤波将其分别提取出来，再将提取出的数据进行叠加还原包络。本文的研究方法和研究结论对DHMC的制备及其在折射率、温度及应变传感中的应用都具有实际的指导意义。

2 原理与仿真

DHMC的干涉原理如图1所示，主要由两个输

收稿日期：2022-07-13；**修回日期**：2022-08-15；**录用日期**：2022-09-07；**网络首发日期**：2022-09-19

基金项目：国家自然科学基金（61875026）、重庆英才青年拔尖人才计划（cstc2021ycjh-bgzxm0128）、重庆英才创新领军人才计划（cstc2021ycjh-bgzxm0287）、重庆市教委科学技术研究重点项目（KJZD-K202201106）、重庆理工大学研究生科研创新项目（gzlcx20223068）

通信作者：*luobinbin@cqut.edu.cn；**zmf@cqut.edu.cn

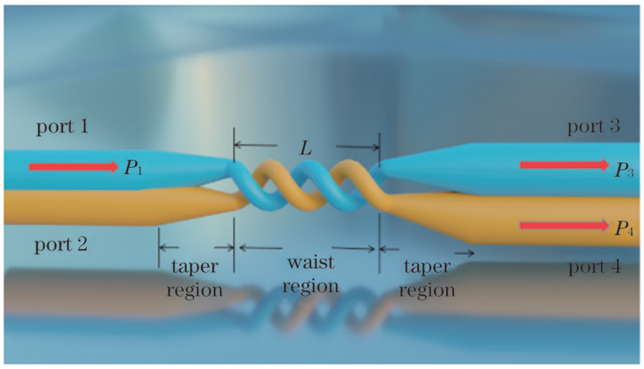

图 1　双螺旋微纳光纤耦合器结构示意图

Fig. 1　Schematic diagram of DHMC structure

入端口、两个输出端口、两个锥形过渡区域和均匀腰区组成，其中腰区部分两根微纳光纤双绞紧密缠绕在一起。两个输入端口是等效的，这里选择端口 1 作为输入端口，当 x、y 偏振的入射光从端口 1 发射时，偶数模和奇数模同时被激发，根据超模理论，两个平行的微纳光纤可视为一个新的波导，当这两种模式沿腰部传播时，它们之间会发生耦合。由于 DHMC 是高度双折射的，因此会在输出端得到两列干涉周期略有不同的 x 方向与 y 方向正交偏振的干涉谱的叠加，从而形成游标包络[20]。输出功率的计算公式为[18]

$$P_3 = P_{1x}\cos^2\left(\frac{1}{2}\phi_x\right) + P_{1y}\cos^2\left(\frac{1}{2}\phi_y\right), \tag{1}$$

$$P_4 = P_{1x}\sin^2\left(\frac{1}{2}\phi_x\right) + P_{1y}\sin^2\left(\frac{1}{2}\phi_y\right), \tag{2}$$

式中：P_{1x}、P_{1y} 分别表示端口 1 在 x、y 偏振方向上的输入光功率；P_3、P_4 分别表示端口 3、端口 4 的总输出功率；ϕ_x 和 ϕ_y 分别表示沿耦合长度积累的奇、偶模的相位差，近似表示为

$$\phi_x = \frac{2\pi L\left(n^x_{\mathrm{even}} - n^x_{\mathrm{odd}}\right)}{\lambda}, \tag{3}$$

$$\phi_y = \frac{2\pi L\left(n^y_{\mathrm{even}} - n^y_{\mathrm{odd}}\right)}{\lambda}, \tag{4}$$

式中：n^x_{odd}、n^x_{even} 和 n^y_{odd}、n^y_{even} 分别为 x 偏振和 y 偏振下奇、偶超模的有效模式折射率(ERI)，可通过 COMSOL 仿真计算得到[19]；L 和 λ 表示耦合区域的长度和入射光波长。

假设入射光在两个偏振中具有相等的光功率，$P_{1x}=P_{1y}=\frac{1}{2}$，通过组合式(1)、式(3)和式(4)，可得端口 3 的输出功率为

$$P_3 = \frac{P_1}{2}\left(1 + \cos\frac{\phi_x - \phi_y}{2}\cos\frac{\phi_x + \phi_y}{2}\right)。 \tag{5}$$

P_3、P_4 输出光谱的下包络函数公式可表示为[18]

$$F_c = \frac{P_1}{2}\left(1 - \left|\cos\frac{\phi_x - \phi_y}{2}\right|\right) = \frac{P_1}{2}\left(1 - \left|\cos\frac{\pi L\left(\Delta n^x_{\mathrm{eff}} - \Delta n^y_{\mathrm{eff}}\right)}{\lambda}\right|\right), \tag{6}$$

式中：$\Delta n^x_{\mathrm{eff}} = n^x_{\mathrm{even}} - n^x_{\mathrm{odd}}$，$\Delta n^y_{\mathrm{eff}} = n^y_{\mathrm{even}} - n^y_{\mathrm{odd}}$ 由式(1)、式(2)可知。

端口 3 和端口 4 输出功率只是相位相差 $\pi/2$，所以此处将 P_3 作为输出端口进行研究。通过 COMSOL 建立模型，有效折射率设置为单模光纤的包层折射率 1.4628，波长 λ 范围为 1250～1650 nm，DHMC 直径 d=4 μm，外部折射率(SRI)分别设置为 1 和 1.333，计算结果分别如图 2(a)和图 2(b)所示。图 2 插图中的外侧大圆表示外界环境层。

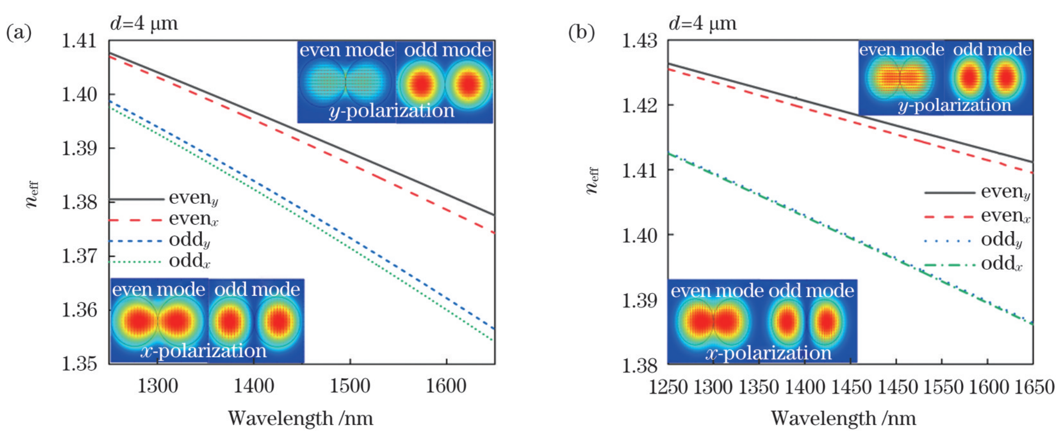

图 2　x 偏振和 y 偏振中的奇、偶模 ERI 计算结果。(a) SRI 为 1；(b) SRI 为 1.333。插图为两种偏振态下的奇、偶模模场分布图

Fig. 2　Calculated results of ERIs of guided even and odd modes in x-polarization and y-polarization. (a) SRI is 1; (b) SRI is 1.333. Insets show modal fields of odd and even modes of two polarizations

由图 2 可见，在 x 和 y 偏振态下，偶模的 ERI 略高于奇模，且随着波长的增加，所有的 ERI 都变小。此外，奇模的 x 偏振和 y 偏振的 ERI 下降趋势是一致的，而偶模的 ERI 之间的差异随着波长的增加而增大，因此，根据式(6)可以推断出偶模对相位差有主要贡献。x、y 偏振态作用下的干涉光谱自由光谱范围(FSR，R_{FS})公式为

$$R_{FS\_x} = \frac{\lambda^2}{\Delta n_{eff}^x L}, \quad (7)$$

$$R_{FS\_y} = \frac{\lambda^2}{\Delta n_{eff}^y L}。 \quad (8)$$

由此可得出 x、y 偏振态叠加的游标包络自由光谱范围公式为

$$R_{FS} = \frac{R_{FS\_x} R_{FS\_y}}{\left| R_{FS\_x} - R_{FS\_y} \right|} = \frac{\lambda^2}{L \left| \Delta n_{eff}^y - \Delta n_{eff}^x \right|}。 \quad (9)$$

图 3 是根据式(3)~式(5)仿真得到的直径 d=4 μm 但腰区长度不同的 DHMC 在空气(SRI 为 1)和液体环境(SRI 为 1.333)中的光谱。由式(9)可知,包络的 FSR 与腰长、波长及 x、y 偏振态下的有效折射率差有关,腰长 L 对 FSR 起主要作用,L 增大,FSR 减小。结合图 2 仿真的 x 偏振和 y 偏振下奇偶模折射率差的变化趋势,可得出:L 一定时,若 SRI 为 1,则随着波长增加,有效折射率差的绝对值增大的速度大于波长平方增加的速度,包络 FSR 也随之减小;当 SRI 大于等于 1.3310 时正好相反,包络 FSR 随波长增加而增大。

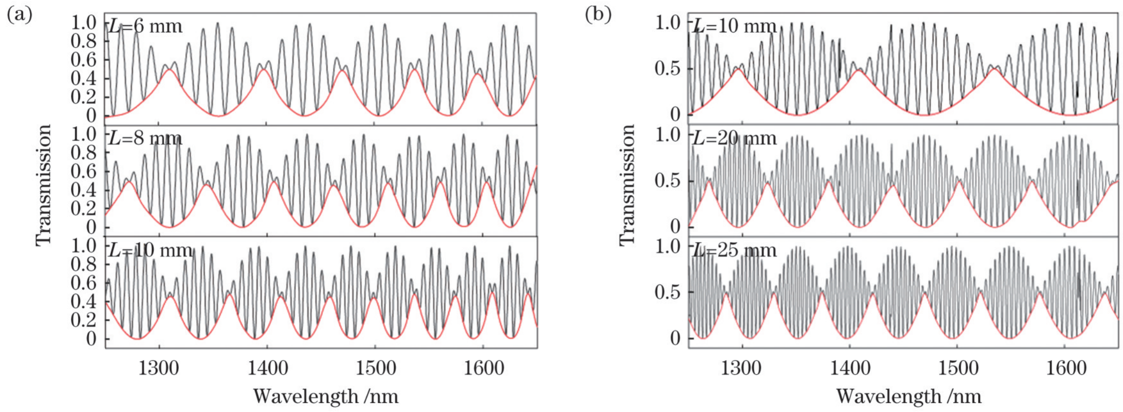

图 3 不同腰区长度 L 的 DHMC 的游标光谱仿真结果(d=4 μm)。(a)SRI 为 1;(b)SRI 为 1.333

Fig. 3 Calculated results of interference spectra with vernier effect for DHMC with different waist lengths L (d=4 μm). (a) SRI is 1; (b) SRI is 1.333

图 4 所示为 DHMC 的包络 FSR 与其直径的关系的仿真结果。由图 4 可见,在相同 SRI(1.3328)下,随着 DHMC 直径的增大,x 和 y 偏振态的奇偶模折射率差减小,FSR 增大;在液体环境中(SRI 为 1.3328),当 DHMC 直径为 6 μm 时,在 1250~1650 nm 的波长范围内都只能观察到一个完整的游标包络。因此,在将 DHMC 运用到折射率、温度或应变传感时可根据图 3、图 4 仿真结果辅助制备具有合适的直径和干涉长度的 DHMC 传感器。此外,Chen 等[19]研究表明随着匝数增加,游标光谱 FSR 逐渐减小,而且传感器检测灵敏度与匝数关系不大,主要取决于耦合器直径,匝数只影响模式的传输相位,而不影响光传输的模式分布。本研究中所制作的光纤耦合器匝数是 4 匝。

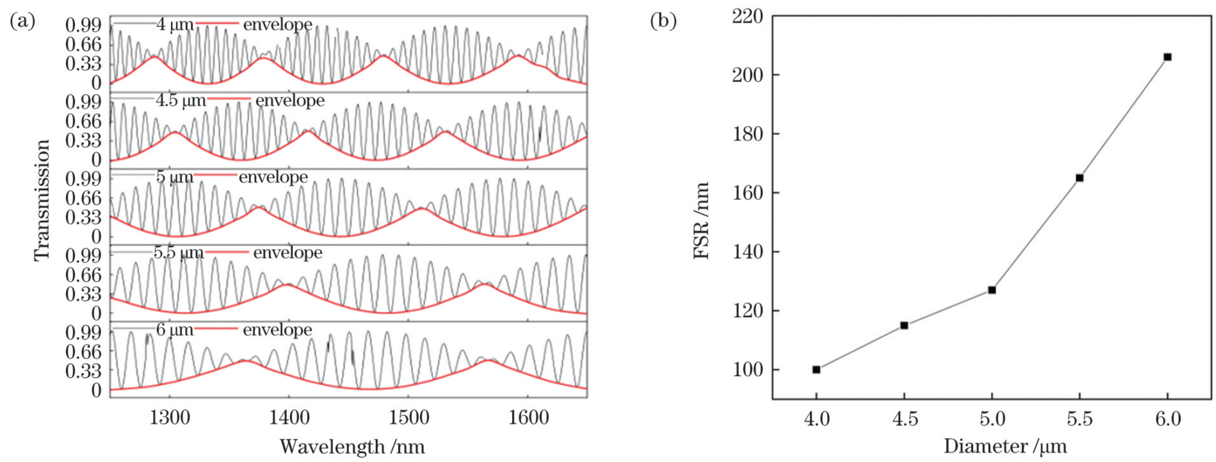

图 4 DHMC(L=12 mm)的 FSR 仿真结果。(a)不同直径 DHMC 透射光谱,SRI 为 1.3328;(b)FSR 与 DHMC 直径的关系

Fig. 4 Simulation results of FSR of DHMC (L=12 mm). (a) Transmission spectra of DHMC with different diameters with SRI of 1.3328; (b) relationship between FSR and diameter of DHMC

3 实验与讨论

3.1 传感器的制备

实验中DHMC由两根标准单模光纤(SMF-28)采用熔融拉锥法制备。首先将两根单模光纤剥掉涂覆层，沿平行方向双绞缠绕，从而获得具有不同匝数的螺旋结构；采用光纤拉锥机(OB-612)对其进行拉锥，光纤两端接上宽带光源(BBS，1250~1650 nm)和光谱分析仪(OSA，AQ6370D)，在拉锥过程中实时观测DHMC的光谱，以便在线估计所制备的DHMC直径和腰区长度。图5(a)和图5(b)分别为DHMC拉锥前后的显微图，图5(c)为DHMC拉锥后在空气中的光谱图，在波长范围1250~1650 nm出现了8个完整的游标下包络峰。仿真结果图3(a)显示，当d=4 μm，L分别为8 mm和10 mm，波长范围为1250~1650 nm时，出现了7个和9个完整的游标包络；当L=10 mm时，1400 nm附近的FSR约为50 nm。图5(c)显示1400 nm附近的FSR为52 nm，并且随着波长增加，FSR逐渐由58 nm减小到40 nm，这也与图3(a)的仿真结果相符。由此，在制备DHMC过程中可大致估计图5(c)的光谱对应的腰区直径约为4 μm，长度在8~10 mm之间。图5(b)是制备好之后DHMC耦合区螺旋结构的显微图。基于图5(b)测出实际DHMC的直径为4 μm，腰部区域长9.6 mm，与理论分析结果基本吻合。

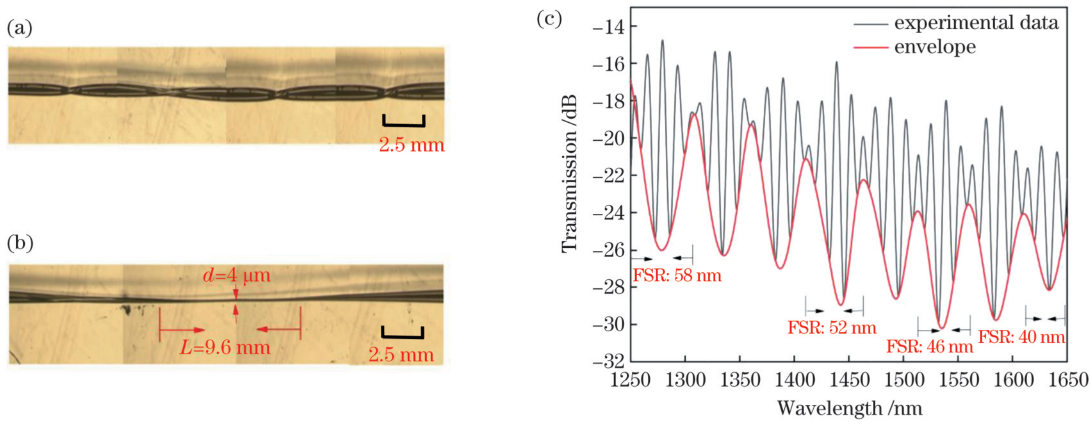

图5 DHMC传感器及其光谱图。(a)加热前的显微图；(b)拉锥后的显微图；(c)拉锥后的DHMC在空气中的光谱图

Fig. 5 DHMC sensor and its spectrum. (a) Microscopic image before heating; (b) microscopic image after tapering; (c) spectrum in air for DHMC after tapering

3.2 轴向应变传感实验

实验中制备了d=6、6.5、7 μm的DHMC进行应变实验，固定在精度为1 μm的精密位移台上，两端分别连接宽带光源和光谱分析仪，然后其中一个位移平台固定不动，另一个位移平台进行轴向位移。实验中将DHMC紧贴在位移台上，施加的轴向应变依次为2000、4000、6000、8000 με。图6(a)为d=6 μm、L=10 mm的DHMC光谱随轴向应变的演变图，随着应变升高，光谱发生蓝移。为进一步分析具有游标效应与无游标效应的DHMC轴向应变灵敏度，对光谱数据进行FFT，在频谱中找出最主要的两个干涉峰，并利用带通滤波法对特征干涉光谱数据进行提取，分别得到在x、y偏振态下以及x、y偏振态叠加下的光谱，如图6(b)~图6(d)所示，可见在施加的轴向应变增大时，x、y偏振态的干涉谱蓝移，而叠加形成的游标包络红移，且漂移量比x、y偏振态下的蓝移漂移量低。图6(e)为d=6 μm的DHMC分别在x、y偏振态下及x、y偏振态叠加下形成光谱的轴向应变灵敏度标定结果：三个应变灵敏度分别为−7.1 pm/με、−10.7 pm/με和4.5 pm/με。再采用相同的实验和数据处理方法对d=6.5 μm和d=7 μm的DHMC分别进行研究，得到d=6.5 μm的DHMC的三个应变灵敏度分别为−4.3 pm/με、−5.8 pm/με和3.5 pm/με，d=7 μm的DHMC的三个应变灵敏度分别为−4 pm/με、−5.1 pm/με和3.1 pm/με，如图6(f)所示。由此可见，DHMC的应变灵敏度与Li等[21]研究的微纳光纤在直径2.5 μm时的应变灵敏度(4.84 pm/με)相比较具有一定优势，可通过干涉光谱信号提取的方式获得单个x、y偏振下更高的应变灵敏度。

3.3 温度传感实验

实验中制备了d=6 μm和d=7 μm的DHMC进行温度特性实验。图7(a)为d=6 μm的DHMC光谱随温度变化的演变图，采取与上述应变传感实验相同的数据处理方法，分别得到在x、y偏振态下以及x、y偏振态叠加下的光谱，如图7(b)~图7(d)所示，可见当温度增加时，x、y偏振态的干涉谱蓝移，而叠加形成的游标包络红移，且漂移量比x、y偏振态下的蓝移漂移量低。图7(e)所示为d=6 μm的DHMC分别在x、y偏振态下的干涉光谱及x、y偏振态叠加下形成的游标光谱的温度灵敏度，分别为−1.742 nm/K、−2.48 nm/K和1.035 nm/K；图7(f)所示d=7 μm的DHMC的三个

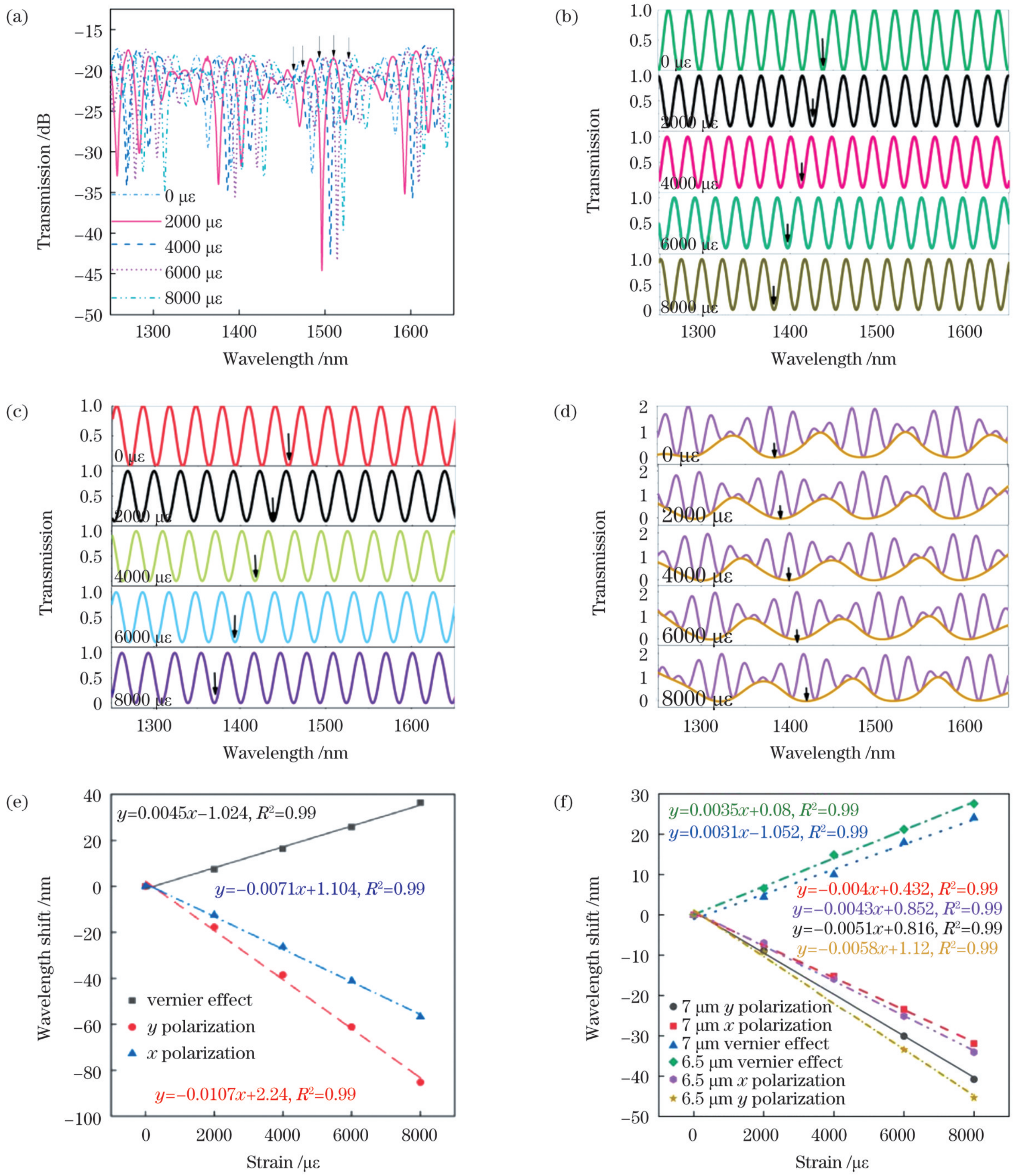

图 6　轴向应变传感实验结果。(a)直径 6 μm、L=10 mm 的 DHMC 在不同轴向应变下的光谱；(b)x 偏振态下 DHMC 光谱随应变漂移；(c)y 偏振态下 DHMC 光谱随应变漂移；(d)游标光谱随应变漂移；(e)直径 6 μm 的 DHMC 轴向应变灵敏度；(f)直径 6.5 μm 和 7 μm 的 DHMC 轴向应变灵敏度

Fig. 6　Experimental results of axial strain sensing. (a) Spectrum evolution of DHMC (L=10 mm) with diameter of 6 μm under different axial strains; (b) spectrum evolution of x polarization with axial strain; (c) spectrum evolution of y polarization with axial strain; (d) evolution of vernier spectrum with axial strain; (e) axial strain sensitivity of DHMC with diameter of 6 μm; (f) axial strain sensitivity of DHMC with diameter of 6.5 μm and 7 μm

温度灵敏度分别为−1.709 nm/K、−2.364 nm/K 和 1.02 nm/K。可见，DHMC 的温度灵敏度与 Sun 等[22]研究的细芯光纤马赫-曾德尔传感器温度灵敏度(−72.89 pm/K)相比具有一定优势，而且可通过提取单个 x、y 偏振态干涉光谱的方式获得更高的温度灵敏度。

3.4 折射率传感实验

折射率传感实验系统如图 8 所示。将制备的 DHMC(d=5 μm，L=10 mm)固定在载玻片上，两端分别连接宽带光源和光谱分析仪，向 DHMC 腰区注入不同折射率的氯化钠溶液，待稳定后观测光谱变化。

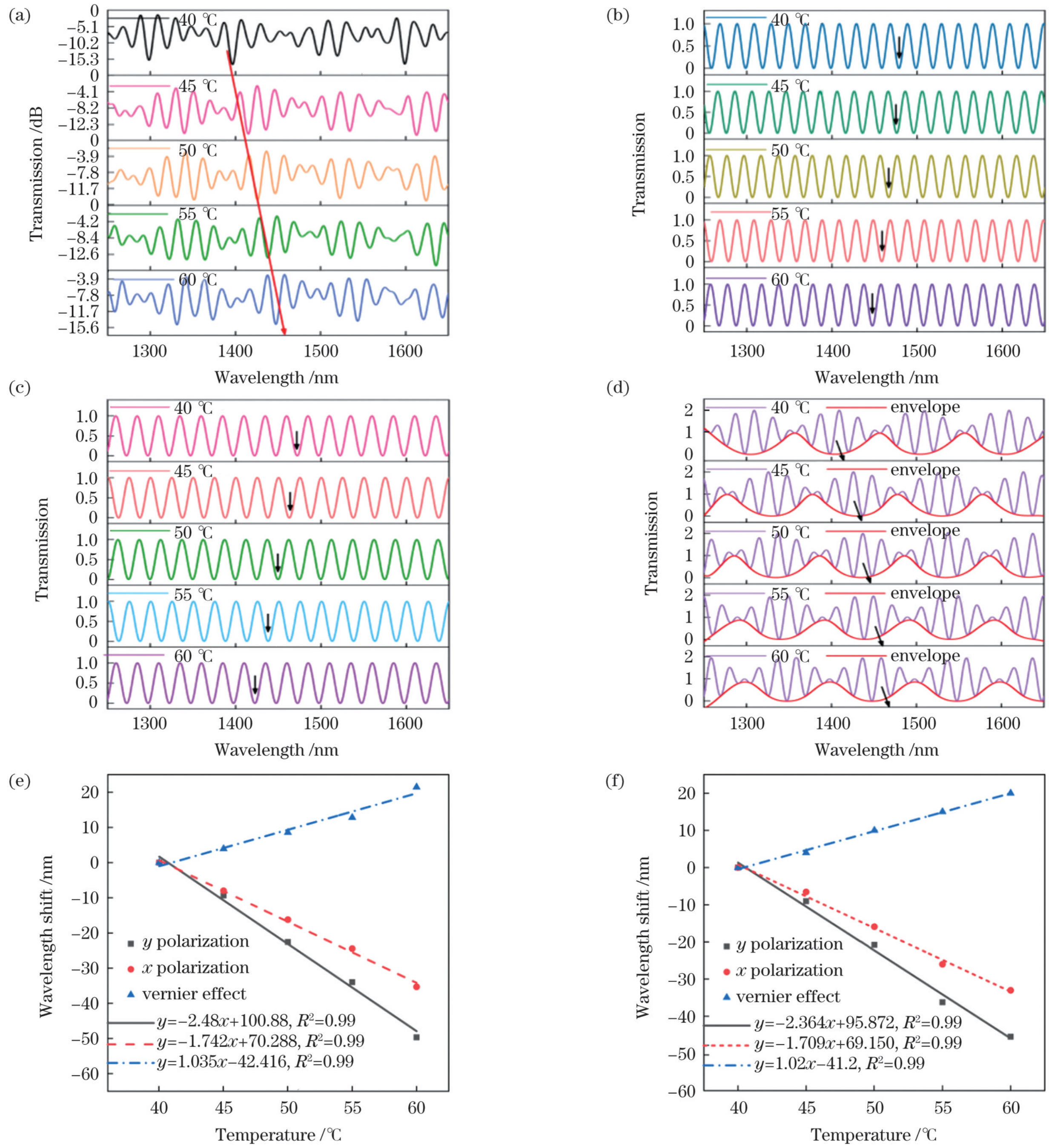

图7 温度传感实验结果。(a)直径6 μm的DHMC在不同温度下的光谱演变；(b)x偏振态下光谱随温度漂移；(c)y偏振态下光谱随温度漂移；(d)游标光谱随温度漂移；(e)直径6 μm的DHMC温度灵敏度；(f)直径7 μm的DHMC温度灵敏度

Fig. 7 Experimental results of temperature sensing. (a) Spectrum evolution with temperature for DHMC with diameter of 6 μm; (b) spectrum evolution of x polarization with temperature; (c) spectrum evolution of y polarization with temperature; (d) evolution of vernier spectrum with temperature; (e) temperature sensitivity of DHMC with diameter of 6 μm; (f) temperature sensitivity of DHMC with diameter of 7 μm

如图9(a)所示，随着SRI的增加，DHMC透射谱发生红移。采用与上述相同的光谱处理方法，分别得到在x、y偏振态下以及x、y偏振态叠加下的光谱，如图9(b)～图9(d)所示。对图9(b)～图9(d)标记的dip A、dip B进行折射率灵敏度分析，得到在x、y偏振态下以及x、y偏振态叠加下的干涉光谱折射率灵敏度标定结果：dip A三个折射率灵敏度分别为7238 nm/RIU、8855 nm/RIU及14429 nm/RIU；dip B三个折射率灵敏度分别为7433 nm/RIU、8944 nm/RIU及14929 nm/RIU。因此，DHMC在有游标效应时的RI灵敏度约是没有游标效应时的2倍，如图9(e)和图9(f)所示。

对以上DHMC的折射率、温度及应变传感特性的分析如下。

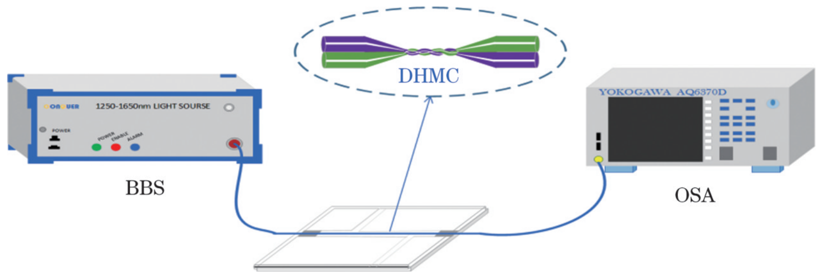

图 8　DHMC 折射率传感实验系统图

Fig. 8　Experimental setup for refractive index measurement using DHMC

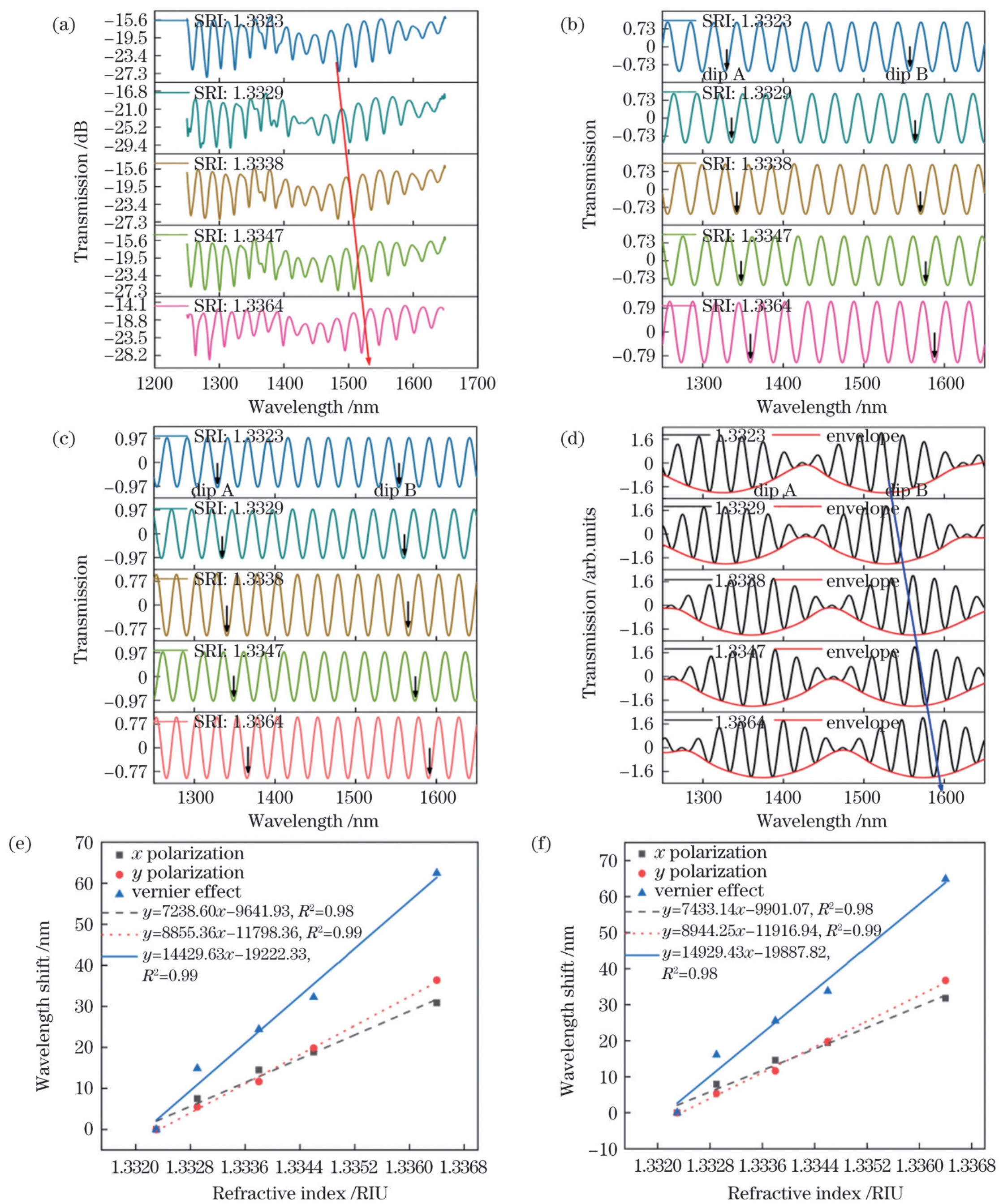

图 9　直径 5 μm 的 DHMC 折射率实验结果。(a)光谱随 SRI 的漂移；(b)x 偏振态下光谱随 SRI 漂移；(c)y 偏振态下光谱随 SRI 漂移；(d)游标包络随 SRI 漂移；(e)dip A 折射率灵敏度；(f)dip B 折射率灵敏度

Fig. 9　Experimental results of DHMC (d=5 μm) for RI sensing. (a) Spectrum evolution with SRI; (b) spectrum evolution of x polarization with SRI; (c) spectrum evolution of y polarization with SRI; (d) evolution of vernier spectrum with SRI; (e) RI sensitivity of dip A; (f) RI sensitivity of dip B

假设M因子为游标包络的FSR和传感干涉谱的FSR之间的比值，在没有特定参考干涉仪的情况下，系统的x、y正交偏振态分别充当传感光谱并互为参考光谱，则游标包络的灵敏度S_{envelope}可用x、y正交偏振态下光谱的FST即$R_{\mathrm{FS_}x}$、$R_{\mathrm{FS_}y}$表示为[23]：

$$S_{\mathrm{envelope}}=\frac{R_{\mathrm{FS\_}y}}{R_{\mathrm{FS\_}y}-R_{\mathrm{FS\_}x}}S_x-\frac{R_{\mathrm{FS\_}x}}{R_{\mathrm{FS\_}y}-R_{\mathrm{FS\_}x}}S_y=M_xS_x-M_yS_y, \tag{10}$$

式中：S_x、S_y分别是DHMC在单独的x、y偏振态下的灵敏度；M_x是x偏振态下的M因子，此时y偏振态被视为参考干涉光谱；M_y是y偏振态下的M因子，此时x偏振态被视为参考干涉光谱。在式(10)中代入x、y偏振态的FSR计算得出的M_x与M_y因子的差异很小。在温度和轴向应变传感中，由于x、y偏振态的灵敏度的绝对差值很小，计算得到M_xS_x与M_yS_y之间的差异相互抵消，因此表现出减弱的光学游标效应；而在折射率传感中，x、y偏振态的折射率灵敏度的绝对差值相比于温度和轴向应变灵敏度的绝对差值大很多，从而M_xS_x与M_yS_y相减大于单个偏振态下的折射率灵敏度，因此表现出增强的光学游标效应。

4 结　　论

DHMC具有灵敏度高、结构紧凑、易制备、成本低等优点。本文详细研究了DHMC的游标效应的内在机理及光谱特性，并分析其对折射率、温度及应变的传感特性。仿真结果表明DHMC的腰长对其游标包络的FSR起主要作用，FSR随着腰区长度的增大而减小，在制备DHMC的过程中，可通过光谱分析仪在线监测DHMC在波长范围1250～1650 nm内包络的个数估计其腰区长度和直径。将DHMC的x与y偏振态干涉谱叠加形成的游标光谱与单个x、y偏振态下的干涉光谱相比较，游标光谱对应变和温度传感呈现出减弱的光学游标效应，而对折射率传感则呈现出增强的光学游标效应。本文的研究结论对于DHMC传感器的制备及其在传感领域的应用具有一定的指导意义。

参 考 文 献

[1] Gao S C, Zhang W G, Bai Z Y, et al. Microfiber-enabled in-line Fabry-Pérot interferometer for high-sensitive force and refractive index sensing[J]. Journal of Lightwave Technology, 2014, 32(9): 1682-1688.

[2] Saha N, Kumar A, Mukherjee A. Enhancement of refractive index sensitivity of Bragg-gratings based optical waveguide sensors using a metal under-cladding[J]. Optics Communications, 2017, 396: 83-87.

[3] Li X G, Warren-Smith S C, Ebendorff-Heidepriem H, et al. Optical fiber refractive index sensor with low detection limit and large dynamic range using a hybrid fiber interferometer[J]. Journal of Lightwave Technology, 2019, 37(13): 2954-2962.

[4] Zhang Y S, Zhang W G, Zhang Y X, et al. Parabolic-cylinder-like long-period fiber grating sensor based on refractive index modulation enhancement effect[J]. Applied Optics, 2019, 58(7): 1772-1777.

[5] Ahsani V, Ahmed F, Jun M B G, et al. Tapered fiber-optic Mach-Zehnder interferometer for ultra-high sensitivity measurement of refractive index[J]. Sensors, 2019, 19(7): 1652-1661.

[6] 彭星玲，李兵，李玉龙. 微纳光纤布拉格光栅折射率与浓度传感器研究进展[J]. 激光与光电子学进展，2018，55(12): 120010.
Peng X L, Li B, Li Y L. Research progress of refractive index and concentration sensors based on micro-nanofiber Bragg grating[J]. Laser & Optoelectronics Progress, 2018, 55(12): 120010.

[7] Li K W, Zhang T, Liu G G, et al. Ultrasensitive optical microfiber coupler based sensors operating near the turning point of effective group index difference[J]. Applied Physics Letters, 2016, 109(10): 101101.

[8] Xu Z L, Sun Q Z, Li B R, et al. Highly sensitive refractive index sensor based on cascaded microfiber knots with vernier effect[J]. Optics Express, 2015, 23(5): 6662-6672.

[9] Bo L, Wang P F, Semenova Y, et al. High sensitivity fiber refractometer based on an optical microfiber coupler[J]. IEEE Photonics Technology Letters, 2013, 25(3): 228-230.

[10] Li K W, Zhang N M Y, Zhang N, et al. Spectral characteristics and ultrahigh sensitivities near the dispersion turning point of optical microfiber couplers[J]. Journal of Lightwave Technology, 2018, 36(12): 2409-2415.

[11] Quan M R, Tian J J, Yao Y. Ultra-high sensitivity Fabry-Perot interferometer gas refractive index fiber sensor based on photonic crystal fiber and vernier effect[J]. Optics Letters, 2015, 40(21): 4891-4894.

[12] 刘福禄，张钰民，庄炜，等. 基于游标效应和基底增敏的复合光纤结构温度传感器[J]. 光学学报，2021，41(15): 1506002.
Liu F L, Zhang Y M, Zhuang W, et al. Fiber temperature sensor with composite structure based on vernier effect and substrate sensitization[J]. Acta Optica Sinica, 2021, 41(15): 1506002.

[13] Zhang J, Liao H, Lu P, et al. Ultrasensitive temperature sensor with cascaded fiber optic Fabry-Perot interferometers based on vernier effect[J]. IEEE Photonics Journal, 2018, 10(5): 6803411.

[14] Nan T, Liu B, Wu Y F, et al. Ultrasensitive strain sensor based on vernier-effect improved parallel structured fiber-optic Fabry-Perot interferometer[J]. Optics Express, 2019, 27(12): 17239-17250.

[15] Zhu H H, Yue Y H, Wang Y J, et al. High-sensitivity optical sensors based on cascaded reflective MZIs and microring resonators[J]. Optics Express, 2017, 25(23): 28612-28617.

[16] Azuelos P, Girault P, Lorrain N, et al. High sensitivity optical biosensor based on polymer materials and using the vernier effect[J]. Optics Express, 2017, 25(24): 30799-30806.

[17] Ren L Q, Zhang X W, Guo X X, et al. High-sensitivity optofluidic sensor based on coupled liquid-core laser[J]. IEEE Photonics Technology Letters, 2017, 29(8): 639-642.

[18] Li K W, Zhang N, Zhang N M Y, et al. Birefringence induced vernier effect in optical fiber modal interferometers for enhanced sensing[J]. Sensors and Actuators B: Chemical, 2018, 275: 16-24.

[19] Chen G T, Zhang Y X, Zhang W G, et al. Double helix microfiber coupler enhances refractive index sensing based on vernier effect[J]. Optical Fiber Technology, 2020, 54: 102112.

[20] 郝晋青，韩丙辰. 基于游标效应的高灵敏度光纤耦合器折射率传感器[J]. 光学学报，2020，40(2): 0206002.
Hao J Q, Han B C. Ultrasensitive refractive index sensor based on optical fiber couplers assisted with vernier effect[J]. Acta Optica Sinica, 2020, 40(2): 0206002.

[21] Li W, Hu Z F, Li X Y, et al. High-sensitivity microfiber strain and force sensors[J]. Optics Communications, 2014, 314: 28-30.

[22] Sun M, Xu B, Dong X Y, et al. Optical fiber strain and temperature sensor based on an in-line Mach-Zehnder interferometer using thin-core fiber[J]. Optics Communications, 2012, 285(18): 3721-3725.

[23] Gomes A, Bartelt H, Frazo O. Optical vernier effect: recent advances and developments[J]. Laser & Photonics Review, 2021, 15(7): 202000588.

Sensing Characteristics of Optical Vernier of Double-Helix Micro-Nano Optical Fiber Coupler

Li Yujie, Luo Binbin*, Zou Xue, Shi Shenghui, Fan Junhao, Wu Decao, Chen Huiji, Yang Xiangwen, Gu Hong, Zhao Mingfu**

Chongqing Key Laboratory of Optical Fiber Sensor and Photoelectric Detection, Chongqing University of Technology, Chongqing 400054, *China*

Abstract

Objective In recent years, vernier effect has attracted much attention in the field of optical fiber sensing due to its sensitivity amplification effect, which has been used to measure gas pressure, temperature, strain, refractive index, etc. The configurations used to introduce optical vernier effects fall into two broad categories. The first type consists of configurations containing a single type of interferometer. The second type consists of a hybrid configuration in which two different types of interferometers are combined. The optical vernier effect can be applied to different types of interference structures, such as Mach-Zehnder interferometers (MZIs), Fabry-Perot interferometers (FPIs) and Sagnac interferometers (SIs), etc. Since the double-helix micro-nano fiber coupler (DHMC) is highly birefringent, the superposition of two orthogonal polarization interference spectra in x direction and y direction with slightly different interference periods can form the vernier envelope. However, how to get the DHMC that can produce the vernier envelope spectrum? What's more, when the optical vernier effect of the DHMC is applied to temperature, strain and refractive index sensing, whether the sensing characteristics are consistent or not is a problem that needs to be considered. In the present study, the internal mechanism and spectral characteristics of the vernier effect of the DHMC are studied theoretically. DHMCs with different diameters are fabricated, and experiments of the strain, temperature and refractive index sensing are carried out. We hope that the above results have a good guiding significance for the preparation of DHMC and the applications of refractive index, temperature and strain sensing.

Methods Theoretical and experimental analysis methods are employed in this paper. Firstly, COMSOL software was used to establish the DHMC simulation model (Fig. 1). Then, by setting parameters such as wavelength range, diameter and refractive index, the effective refractive indices of odd and even modes in x- and y-polarization states were obtained, and then the simulated vernier spectra were obtained through Eqs. (5) and (6). Secondly, two standard single-mode fibers (SMF-28) were used to fabricate DHMC, for which the optical fibers with the coating layer stripped off were twisted in parallel direction to obtain helical structures with different turns. The optical fiber pulling machine (OB-612) was used to pull the DHMC, and the broadband light source (1250–1650 nm) and optical spectrum analyzer (OSA) were connected at both ends of the optical fiber. The spectrum of DHMC was observed in real time during the pulling process, so as to estimate the diameter and waist length of the prepared DHMC online. Thirdly, we used the fabricated DHMC to conduct the strain, temperature and refractive index sensing experiments. The spectrum evolutions of the DHMC under different strain, temperature and surrounding refractive index were recorded, respectively. Fast Fourier transform (FFT) and bandpass filtering method were used to extract the characteristic interference spectra, thus obtaining the spectra in x- and y-polarization states, and then the vernier spectrum was obtained by the superposition of the interference of the extracted x- and y-polarization spectra. At last, the sensitivities of the strain, temperature and refractive index of DHMC for x polarization, y polarization and vernier spectrum were analyzed.

Results and Discussions The free spectral range (FSR) of the vernier spectrum of the DHMC is related to the waist length, wavelength and the difference of effective refractive index between x- and y-polarization states. The waist length L plays a major role in FSR, and the increase of L leads to the decrease of FSR (Fig. 3). It can be concluded that when L is fixed and the surrounding refractive index (SRI) is 1, with the increase of wavelength, the absolute value of the effective refractive index difference increases faster than the increase of wavelength square, and the envelope FSR also decreases [Fig. 3(a)]. When the SRI is larger than 1.3310, the results are the opposite, and the envelope FSR increases accordingly [Fig. 3(b)]. Under the same SRI of 1.3328, the odd-even refractive index difference between x- and y-polarization states decreases and FSR increases with the increase in the diameter of DHMC. In the liquid environment (SRI is 1.3328), when the diameter is 6 μm, only a complete vernier envelope can be observed in the wavelength range of 1250–1650 nm (Fig. 4).

In general, the axial strain sensitivity of vernier spectrum of the DHMC is lower than those of x- and y-polarization spectra (Fig. 6). Similarly, the temperature sensitivities of DHMC in x- and y-polarization spectra are higher than that of vernier spectrum of DHMC (Fig. 7). Conversely, the refractive index sensitivity of vernier spectrum of the DHMC is larger than those of x- and y-polarization spectra (Fig. 9). According to Eq. (10), in temperature and axial strain sensing, because the absolute difference between the sensitivity of x- and y-polarization states is very small, the calculated differences between M_xS_x and M_yS_y cancel out each other, thus showing a weakened optical vernier effect. However, in refractive index sensing, the absolute difference of the refractive index sensitivity of x- and y-polarization states is much larger than that of temperature and axial strain sensitivity. It can be concluded that the subtraction of M_xS_x and M_yS_y is larger than the refractive index sensitivity of a single polarization state, thus showing the enhanced optical vernier effect.

Conclusions DHMC has the advantages of high sensitivity, compact structure, easy preparation and low cost. In this work, the internal mechanism and spectral characteristics of the vernier effect of DHMC are studied in detail, and its sensing characteristics of refractive index, temperature and strain are analyzed. The simulation results show that the waist length of DHMC plays a major role in the FSR of its vernier envelope, and the FSR decreases with the increase of the waist length. In the process of DHMC preparation, the waist length and diameter of DHMC can be estimated by monitoring the number of envelopes in the wavelength range of 1250–1650 nm with the OSA online. The vernier spectrum formed by the superposition of the interference spectra of x- and y-polarization states of DHMC is compared with the interference spectra of single x- and y-polarization states. The vernier spectrum shows a weakened optical vernier effect for strain and temperature sensing, while it shows an enhanced optical vernier effect for refractive index sensing. The conclusion of this paper has a good guiding significance for the preparation of DHMC sensor and its application in the sensing field.

Key words fiber optics; fiber optic sensor; double-helix micro-nano fiber coupler; refractive index; temperature; axial strain